COMMUNICATION

High Open-Circuit Voltages in Tin-Rich Low-Bandgap Perovskite-Based Planar Heterojunction Photovoltaics

Baodan Zhao, Mojtaba Abdi-Jalebi, Maxim Tabachnyk, Hugh Glass, Varun S. Kamboj, Wanyi Nie, Andrew J. Pearson, Yuttapoom Puttisong, Karl C. Gödel, Harvey E. Beere, David A. Ritchie, Aditya D. Mohite, Siân E. Dutton, Richard H. Friend, and Aditya Sadhanala*

The performance of organometallic halide (hybrid) perovskite solar cells has improved dramatically in just a few years, with photovoltaic (PV) power conversion efficiencies (PCEs) now exceeding 22% for state-of-the-art devices.[1–5] This remarkable result, coupled with their low cost, tunability, and versatile low-temperature preparation methods, makes hybrid perovskites one of the most promising semiconductor classes not just for solar energy harvesting, but also for light emitting diodes (LEDs), field effect transistors (FETs), and lasers.[6–12] 3D organometallic halide perovskites such as those studied here adopt the classic perovskite structure ABX_3, where A represents the organic cation like methylammonium (MA); B the divalent metal ion like lead (Pb^{2+}), tin (Sn^{2+}), germanium (Ge^{2+}); and X the halide like chlorine (Cl^-), bromine (Br^-), iodine (I^-), a mixture of halides, or pseudohalide/molecular ions (BF_4^-).[12–17] The vast majority of research conducted in this area has focused on "first generation" $MAPbX_3$-based perovskites,[8,18] mainly due to the excellent tunability of their optoelectronic properties.[18,19] Characteristics such as high mobility,[20,21] high bimolecular recombination rate for charge carriers,[10] and low exciton binding energy[22–24] have resulted in the demonstration of high-performance films and devices for PV, LED,[9,12,25–27] FET,[21] and lasing applications.[10,28] One potential drawback of the $MAPbX_3$ semiconductor family, however, is its relatively wide bandgap (3.2–1.6 eV), which dramatically limits its sensitivity in the near-IR (NIR) to mid-IR region of the solar spectrum. Replacement of Pb^{2+} for Sn^{2+} can extend the absorption range to below 1.3 eV,[13,14] with intermediate bandgaps obtained via the fractional substitution of the original

cation.[29–31] Of relevance to this work is the binary metal perovskite $CH_3NH_3(Pb_xSn_{1-x})I_3$ [$0 \leq x \leq 1$].[30,31] Interestingly, the bandgap bows and becomes lower when Sn^{2+} is substituted by Pb^{2+} for samples with 80% and 60% Sn content compared to 100% Sn-based perovskite, in line with previous observations.[30,31] While such tin-based perovskites offer tunable bandgaps down to 1.1 eV, the fabrication of efficient optoelectronic devices has been impeded by factors including poor semiconductor quality and low surface coverage.[30] As a consequence, solar cells made using these perovskites often exhibit very low efficiencies, with typical PCEs < 1% obtained for planar heterojunction devices.[30]

To overcome this challenge, we have developed a novel elevated temperature processing method (depicted in **Figure 1**A),[32] for preparing $CH_3NH_3(Pb_xSn_{1-x})I_3$ perovskites on a Poly(3,4-ethylenedioxythiophene):poly(styrenesulfonate) (PEDOT:PSS)/nickel oxide (NiO) bilayer, which results in the formation of large micron-sized grains (Figure 1B) with almost complete substrate coverage. Our semiconductors not only exhibit relatively low energetic and structural disorder but also impart high PCEs when fabricated into a PV device. For PVs prepared using the lowest bandgap perovskites, open circuit voltages (V_{OC}'s) approaching the prediction of the Shockley–Queisser (S–Q) model are demonstrated. Such promising performance metrics are obtained against a backdrop of fast radiative recombination and low photoluminescence quantum efficiencies (PLQEs), pointing toward the crucial role of high intrinsic charge carrier mobility in these low-bandgap semiconductors.

To study the optical properties of the $CH_3NH_3(Pb_xSn_{1-x})I_3$ [$0 \leq x \leq 1$] perovskite thin films, linear absorption and photoluminescence (PL) were measured as shown in Figure S1 (Supporting Information). It can be observed in Figure 1C that the bandgap bows as we substitute Pb^{2+} in place of Sn^{2+} (until 40% Sn^{2+} ions are replaced by Pb^{2+}) and results in a non-monotonic bandgap lowering similar to what was observed previously by Hao etal.[31] Briefly, the bandgap of the 60% and 80% Sn content films exhibit a lower bandgap than the 100% Sn-substituted films. A similar trend can also be traced in the PL spectra (see Figure S1B of the Supporting Information) where the PL spectra of 80% and 60% Sn content thin-film samples are red-shifted compared to the 100% Sn content thin-film sample, which is consistent with the absorption spectra. Such anomalous bandgap bowing and lack of conformity with Vegard's law[31,33] have been attributed to the competition

B. Zhao, M. Abdi-Jalebi, M. Tabachnyk, H. Glass, V. S. Kamboj, Dr. A. J. Pearson, Dr. Y. Puttisong, K. C. Gödel, Dr. H. E. Beere, Prof. D. A. Ritchie, Dr. S. E. Dutton, Prof. R. H. Friend, Dr. A. Sadhanala
Cavendish Laboratory
University of Cambridge
JJ Thomson Avenue, Cambridge CB3 0HE, UK
E-mail: as2233@cam.ac.uk
Dr. W. Nie, Dr. A. D. Mohite
Los Alamos National Laboratory
Los Alamos, NM 87545, USA

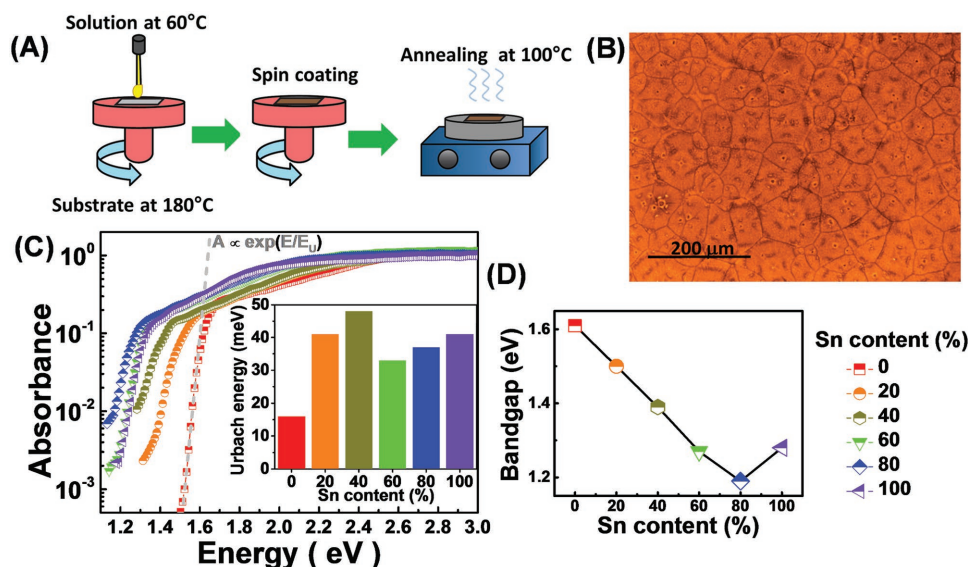**Figure 1.** A) Graphical representation of the elevated temperature processing used to fabricate the $CH_3NH_3(Pb_xSn_{1-x})I_3$ [$0 \leq x \leq 1$] perovskite thin films, and B) the optical microscope image of the large grains and continuous morphology obtained for a typical perovskite thin film. C) PDS spectra of $CH_3NH_3(Pb_xSn_{1-x})I_3$ [$0 \leq x \leq 1$] perovskite thin film with varying Sn content, as indicated, demonstrating the steep fall at the absorption edge. The inset shows the Urbach energy for each of these compositions. D) The change in the bandgap with composition revealing the bandgap bowing effect demonstrated in these perovskites. The bandgaps were estimated using Tauc plots.

between the spin–orbit coupling of the Pb^{2+} and Sn^{2+} ions and further lattice distortions caused in the mixed compositions, i.e., $CH_3NH_3(Pb_xSn_{1-x})I_3$ [$0 < x < 1$].[31,33] The compositions containing 60% and 80% Sn content show lower bandgaps of ≈1.27 and 1.19 eV (as determined by Tauc plots (see the Supporting Information, Figure S2) and corresponding PL peak wavelengths of ≈980 and 1000 nm, respectively, compared to the pure tin perovskite (100% Sn content) that has a bandgap of ≈1.28 eV and a PL peak wavelength of 950 nm. PL for the 40% Sn and 20% Sn content samples could not be measured as the emission was weak potentially due to the highly disordered nature and dominant nonradiative losses as described later.

To analyze the semiconductor quality and estimate the disorder in the $CH_3NH_3(Pb_xSn_{1-x})I_3$ [$0 \leq x \leq 1$] perovskite semiconductor family, we performed sensitive optical absorption measurements using photothermal deflection spectroscopy (PDS) technique. PDS is capable of measuring 4–5 orders of magnitude dynamic range absorption data that allow for assessing the perovskite semiconductor quality and measuring disorder in terms of Urbach energy "E_U" with a higher degree of sensitivity compared to linear absorption measurement techniques.[34–36] Urbach energy can be derived from the following expression:

$$A = A_0 \exp\left((E - E_g)/E_U\right) \qquad (1)$$

where A is the absorbance, A_0 is a constant, and E_g is the bandgap of the material.[34,36] The bandedges are sharp and have a steep fall resulting in low Urbach energies as shown in the inset of Figure 1C. The Urbach energy is the lowest ≈16 meV for the pure lead-based perovskite—$CH_3NH_3PbI_3$ (i.e., 0% Sn content) and is in agreement with previous reports.[34] The 20% and 40% tin content samples show the highest Urbach energy

of ≈41 and 48 meV, respectively, and this is likely due to the lattice distortions and high defect densities in these samples and might be one of the reasons behind their lack of PL. The samples containing higher Sn content (>50% Sn) show a remarkable reduction in the Urbach energies with 60% Sn sample showing the lowest Urbach energy of ≈33 meV among all the binary metal $CH_3NH_3(Pb_xSn_{1-x})I_3$ [$0 < x < 1$] perovskite family. The lowest bandgap (80% Sn content) sample shows Urbach energy of ≈37 meV followed by the pure tin (100% Sn content) sample at ≈41 meV. These values of Urbach energy reflect the contributions from all light-absorbing species, including both band tail states that give rise to charge photogeneration and also states associated with defects and disorder that do not generate photocurrent.[37] These two can be differentiated by parallel measurements of the photocurrent excitation spectra, as we present in **Figure 2**. We find very similar Urbach energies for the pure lead materials (0% Sn content sample) while we observe significant differences for the lead–tin systems, with significantly smaller Urbach energies from the photocurrent measurements (16 and 19 meV for 60% and 80% tin content samples). This demonstrates that there are additional sub-bandgap states for these mixed systems, which could, in principle, provide efficient quenching sites for photogenerated carriers and may even be responsible for the monomolecular decay kinetics in luminescence.[38] This becomes more important in the case of Sn-based perovskites where doping due to easy oxidation of Sn^{2+} to Sn^{4+} is a dominant factor in determining the resultant semiconductor quality and also the diffusion lengths of the photogenerated charge carriers.[13,14,39] As we have shown below, there is little evidence that these quenching sites play such a role in the materials demonstrated in our work. It is possible therefore that they are not in a good electronic contact with the bulk material.
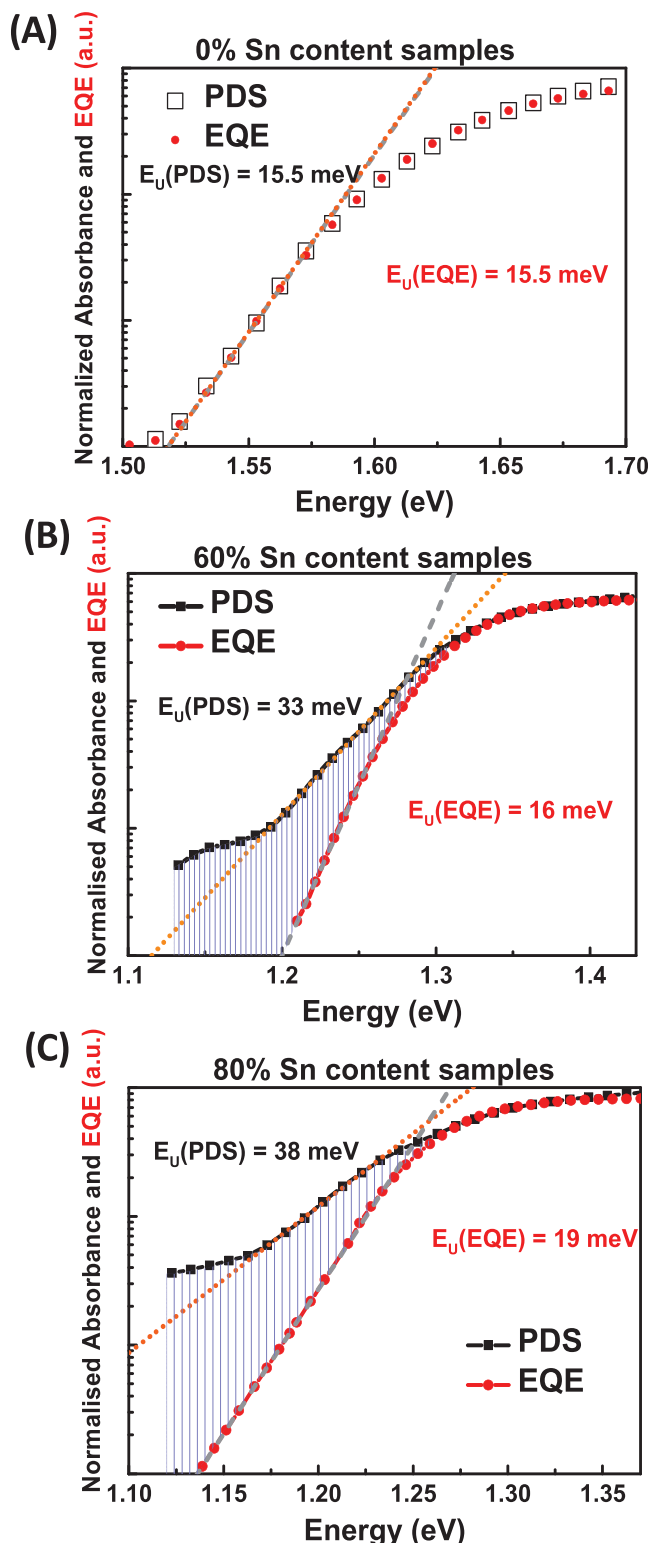
ADVANCED
SCIENCE NEWS
www.advancedsciencenews.com

ADVANCED
MATERIALS
www.advmat.de

COMMUNICATION

Figure 2. A–C) The normalized PDS and the EQE spectra of 0%, 60%, and 80% Sn content samples, respectively. The shaded region indicates the difference between EQE and PDS spectra that signifies the states which do not cause charge generation. The estimated Urbach energies obtained from PDS- and EQE-based measurements are stated for each sample. The EQE was measured using in the following PV device configuration—ITO/PEDOT:PSS/NiO/CH$_3$NH$_3$(Pb$_x$Sn$_{1−x}$)I$_3$/PC$_{61}$BM/Al.

The X-ray diffraction patterns of the CH$_3$NH$_3$(Pb$_x$Sn$_{1−x}$)I$_3$ [$0 \leq x \leq 1$] based thin-film perovskite samples are presented in Figure S3A (Supporting Information) and the refined space group and lattice parameters are given in Table S1 (Supporting Information). Quantitative analysis to determine the symmetry and lattice parameters was carried out using a Le Bail analysis,[40] in the Fullprof Suite of programmes,[41] since preferential alignment in the films prevents a full analysis of the crystal structure. In all samples, a secondary chloride containing phase, MAMCl$_3$, is observed (where MA is CH$_3$NH$_3$ and M is Pb and/or Sn). This is a result of the use of a methylammonium chloride (MACl) reagent, which, we postulate, facilitates the growth of large crystals. The lead film, CH$_3$NH$_3$PbI$_3$, was modeled using I4cm tetragonal structure and CH$_3$NH$_3$SnI$_3$ was modeled with a higher symmetry P4mm pseudocubic structure. As can be seen in Figure S3A (Supporting Information), films with higher tin contents have an additional peak at $2\theta \approx 25°$. This corresponds to the (111) reflection in the P4mm space group but is absent in I4cm symmetry films. The (111) reflection is present in compositions with up to 40% Sn in agreement with previous reports of mixed Pb/Sn films.[31] Changes in the size of the unit cell across the solid solution can be compared most readily by considering the pseudocubic lattice parameters, defined as:

$$a_{pc} = a_{P4mm}, c_{pc} = c_{P4mm} \tag{2}$$

$$a_{pc} = a_{I4cm}/\sqrt{2}, c_{pc} = c_{I4cm}/2 \tag{3}$$

These are plotted as a function of composition in Figure S3B (Supporting Information). The changes in the lattice parameter are approximately linear with composition and so do not correlate with the nonlinear changes in the band gap. Changes to the crystal structure can also be probed by considering how the tetragonal distortion, changes with composition, shown in Figure S3C (Supporting Information):

$$\%\text{tetragonal distortion} = 2(c_{pc} - a_{pc})/(a_{pc} + c_{pc}) \tag{4}$$

The extent the tetragonal distortion changes dramatically as the symmetry changes and follows a similar trend to the changes in the band gap (Figure S3C, Supporting Information). Our measurements are not sensitive to the changes in the positions in the atomic coordinates which are known to influence the electronic properties of perovskites,[42,43] and so we cannot directly probe the rotation of the MI$_6$ octahedra or the M ion displacement across the composition series. However, previous analysis of distortions in perovskites[44] has shown that in the lower symmetry I4cm space group both cation displacement and octahedral tilting are allowed, whereas in the pseudocubic P4mm space group there are no allowed octahedral tilts. Furthermore, analysis has shown that the extent of the structural distortion is larger in MAPbI$_3$ compared to MASnI$_3$.[31] Structural characterization using powder diffraction would enable us to explore this further in our samples.

We fabricated planar heterojunction PV devices employing these thin films. **Figure 3**A indicated the device structure adopted in this work on top of indium–tin oxide (ITO) substrates—ITO/PEDOT:PSS/NiO/CH$_3$NH$_3$(Pb$_x$Sn$_{1−x}$)I$_3$/
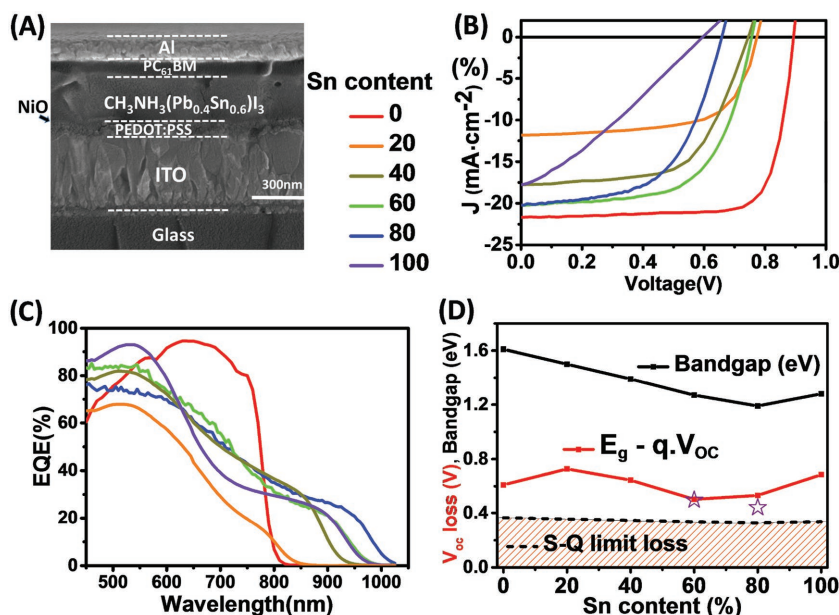
COMMUNICATION

Figure 3. A) The device structure used to fabricate the $CH_3NH_3(Pb_xSn_{1-x})I_3$ [$0 \leq x \leq 1$] perovskite thin-film-based PVs. B) The current density–voltage (J–V) characteristics of these perovskite PV devices with varying Sn content as indicated. C) The external quantum efficiencies (EQEs) for perovskite PV devices with varying Sn content. D) The V_{OC} loss compared to the bandgap ($E_g - qV_{OC}$). The effective loss in V_{OC} from the thermodynamic limit, taking into account the PLQE, is indicated by the star symbol. This shows that the V_{OC} loss from the thermodynamic limit seen for 60% Sn content perovskite PV device is only due to low PLQE.

performance parameters are summarized in **Table 1**. Note that all the devices were measured at 1 sun (≈100 mW cm^{-2}) light intensities. The 0% Sn content based PV devices outperform the other devices with PCE reaching ≈14%. The 100% Sn content based PV device performed least efficiently with PCE reaching only ≈3.2%. Among the binary metal containing perovskites 60% Sn-containing perovskite-based PV devices obtained the best performance with PCEs reaching ≈10% with an open-circuit voltage (V_{OC}) of ≈0.77 V, and the lowest bandgap – 80% Sn content binary metal perovskite-based PV device reached a PCE ≈7.6 % with V_{OC} reaching ≈0.66 V. Both the 60% and 80% Sn content based PVs demonstrate negligible hysteresis (hysteresis data for all the PV devices can be found in the Supporting Information, Figure S8). To the best of our knowledge, these are one of the highest efficiencies achieved so far for Sn-rich binary metal perovskite compositions.[30,31,45–47] Such high efficiencies could be a result of better semiconductor quality in the 60% and 80% Sn content perovskites as inferred from the lower Urbach energies for these compositions compared to other Sn-based perovskites in the family and also the better morphology of perovskite thin films compared to earlier reports.[30] Especially, for the low-bandgap perovskite (60% and 80% Sn content) based PV devices, the obtained V_{OC}'s are significantly high given the fact that planar heterojunction-based PV device configuration is generally known to demonstrate low V_{OC}'s in comparison with device architectures incorporating mesoporous charge extraction layers.[35,48,49] The EQEs measured for these devices are lower at higher wavelengths due to lower absorption in the IR absorption compared to that in the visible region (see the Supporting Information, Figure S1) and this could potentially limit the J_{SC}'s that we get in our devices. This problem has been attributed to the presence of MAPb$_x$Sn$_{1-x}$Cl$_3$ up to 33% of the total material in the thin film that does not absorb visible light due to its large bandgap (>3 eV),[50] and the longer wavelength absorption and EQE can be increased by adding molecular iodine into the precursor solution that reduces this pure chloride perovskite phase to below 10%, hence, enhancing the longer

phenyl-C61-butyric acid methyl ester (PC$_{61}$ BM)/Al. This structure is compatible with low-temperature solution processable technologies like roll-to-roll printing, while the conventional TiO$_2$ and 2,2′,7,7′-Tetrakis-(N,N-di-4-methoxyphenylamino)-9,9′-spirobifluorene (Spiro-OMeTAD)-based structures need high processing temperatures (e.g., 500 °C) making it difficult to work with flexible substrates like polyethylene terephthalate. The combination of ITO/PEDOT:PSS/NiO acts as a hole-selective contact for the perovskite as well as an electron blocking layer, and the combination of PC$_{61}$BM/Al forms the electron selective contact for the perovskite along with acting as a hole-blocking layer. Figure 3B,C illustrates the photocurrent density–voltage (J–V) scans measured with a calibrated AM 1.5 source (1 sun) and the corresponding external quantum efficiency (EQE) for the PV devices with different Sn content fabricated by an elevated temperature processing method as described earlier. The device

Table 1. The performance parameters achieved for the $CH_3NH_3(Pb_xSn_{1-x})I_3$ [$0 \leq x \leq 1$] perovskite thin-film-based PVs for the best devices. Predicted J_{SC} values obtained from EQE are not measured in the UV region below 450 nm and hence the estimated J_{SC} values are slightly lower than the actual J_{SC} measured under a standard AM 1.5 light. Statistical average PCE values are also stated in the brackets.

Sn content [%]	V_{oc} [V]	J_{sc} [mA cm^{-2}]	FF [%]	PCE (Avg. PCE) [%]	J_{sc} (from EQE) [mA cm^{-2}]
0	0.902	21.0	76.6	14.4 (13.8)	20.5
20	0.773	11.8	65.0	5.9 (5.6)	11.1
40	0.745	17.8	61.6	8.2 (7.3)	17.1
60	0.767	20.5	63.1	10.0 (9.2)	20.0
80	0.658	20.2	56.9	7.6 (6.5)	19.5
100	0.595	17.8	29.8	3.2 (2.1)	17.6

wavelength absorption.[50] This is beyond the scope of the current work and is being investigated separately.

Now, taking into account the PLQE of these materials at 1 sun intensity (0.0007 ± 10^{-5} and 0.009 ± 10^{-4} for 60% and 80% Sn content thin films, respectively) the V_{OC} loss was estimated, using $kT\ln$ (PLQE),[51–53] to be ≈200 and 120 meV, respectively for 60% and 80% Sn content based PVs. Now, if we account for this loss from the maximum thermodynamically achievable V_{OC}'s for the 60% and 80% Sn content based PVs (0.97 and 0.89 V, respectively, with respect to their bandgaps) yields a V_{OC} of around ≈0.77 V and 0.77 V, respectively. We emphasize that, remarkably, the measured V_{OC} value for the 60% Sn content matches with the estimated maximum thermodynamically achievable V_{OC}'s suggesting that we do not have any additional loss other than the losses due to the low PLQEs which can possibly be attributed to the superior semiconductor quality we achieve using elevated temperature processing of perovskite. However, for the 80% Sn content PV device there is still an additional loss of ≈110 meV that can potentially arise from the defects present in this perovskite and poor quality of morphology compared to the 60% Sn content sample (see the Supporting Information, Figure S9). Therefore, further improvements in the V_{OC}'s in these systems can possibly come from improvement of the PLQEs, paving the way for V_{OC}'s close to the values predicted from the S–Q model.

The V_{OC} loss from the bandgap ($E_g - qV_{OC}$) is plotted in the Figure 3D along with the predicted V_{OC} values using the S–Q model for each bandgap.[52] The S–Q limit of V_{OC} changes for different bandgaps and has been adapted from Nayak and Cahen.[52] We can observe that for the 60% and 80% Sn content devices if we consider the losses due to the low PLQEs, the 60% Sn devices do not show any additional losses. We measured the PL lifetimes for 60% and 80% Sn content samples at an excitation density of ≈5×10^{15} cm^{-3} (similar to the charge carrier density ≈1 sun) and we obtain lifetimes of 0.87 and 0.95 ns, respectively, with the decay fitted using the monomolecular recombination model (see the Supporting Information, Figure S10 and Table S2). The PL decay lifetimes for the 100% Sn sample were within the instrument limit of 0.3 ns. Such low PL lifetimes especially for the 60% and 80% Sn content samples along with the low PLQE values point toward highly dominant nonradiative processes and should have resulted in very poor PV performances. However, we observe very efficient performance from the 60% and 80% Sn content based perovskite PVs. This is only possible when the intrinsic mobilities are high because that enables efficient charge separation and prevents charge carrier recombination. To validate this, we performed terahertz pump-probe measurements that can probe intrinsic charge carrier mobility values in a thin film.[20] We obtained high charge carrier mobility values in the range of 100–200 cm^2 V^{-1} s^{-1} for perovskite thin-film samples with Sn content >50%, which might be the reason behind the remarkable performance of the low-bandgap perovskite PVs.[39] More details are available in the Supporting Information, Figure S11 and Table S3.

To further elucidate the charge recombination processes in $CH_3NH_3(Pb_xSn_{1-x})I_3$ [$0 \le x \le 1$] perovskite-based PV devices, we performed light-intensity-dependent PV characterization measurement on the 60% and 80% Sn content perovskite-
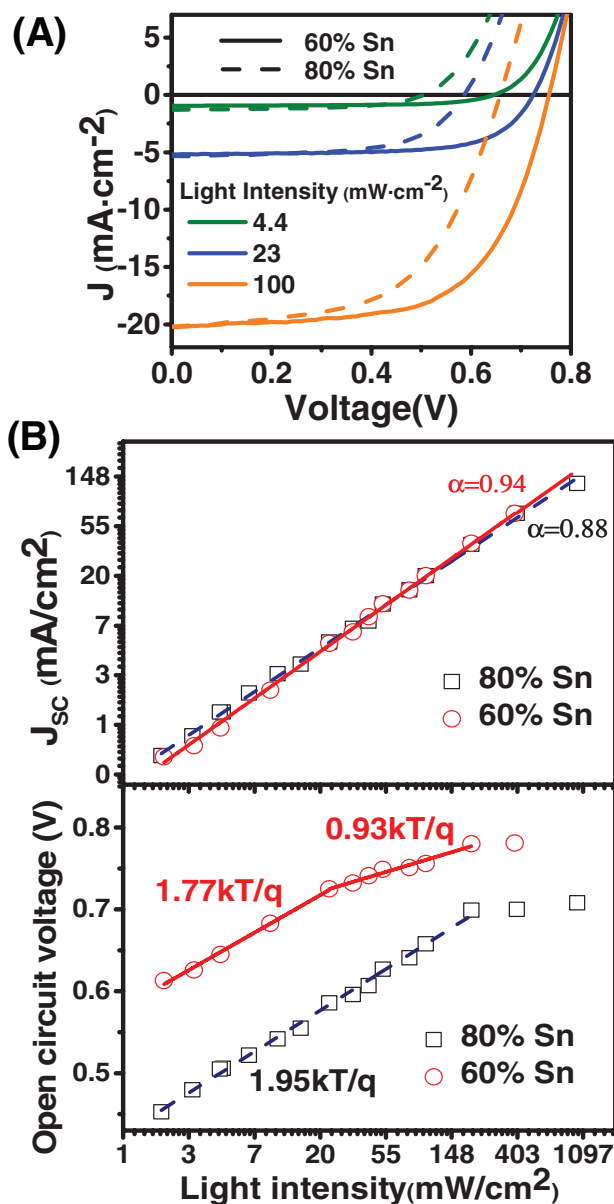

Figure 4. A) J–V curves of 60% and 80% Sn content perovskite PV device under different light intensity (I). B) Short-circuit current (J_{SC}) and open-circuit voltage (V_{OC}) of 60% and 80% Sn content perovskite PV device plotted against incident light intensity.

based PVs. **Figure 4**A illustrates J–V curves of the 60% and 80% Sn content PVs under different incident light intensity from 0.02 to 1 sun (for a complete set of J–V curves, please see the Supporting Information, Figure S12). The J–V curves are almost parallel to the x-axis (voltage axis) around the J_{SC} (voltage = 0 V) indicating that the series resistance has no effect on J_{SC} in these two devices. Furthermore, the J_{SC} and V_{OC} at these different light intensities are captured in Figure 4B. Figure 4B (top) demonstrates the power law dependence, $J \propto I$, of the J_{SC} on incident light intensity, where the data are plotted on a log–log scale. The 60% Sn content based perovskite PV demonstrates an =0.94 that is close to unity, indicating that there are no significant energy barriers and space charge limits

COMMUNICATION

for the charge extraction process.[54,55] On the other hand, for the 80% Sn content based perovskite PV that demonstrates a relatively smaller value of = 0.88 compare to the 60% Sn content based perovskite PV, this points toward the presence of space charge limitations in this device possibly due to poor thin-film coverage issues compared to its 60% Sn content counterpart (see the Supporting Information, Figure S9).

The light-intensity-dependent V_{OC} provides critical insights into the mechanism of recombination processes in the PV device. At V_{OC} there is no net flow of current ($J = 0$ mA cm^{-2}), which means that all the photogenerated charge carriers should recombine in the perovskite film. The corresponding charge carrier recombination process is reflected by the value of "n" determined by the slope of the V_{OC} versus incident light intensity; $n(kT/q)$ where q is the elementary charge, k is the Boltzmann constant, and T is the temperature.[56,57] V_{OC} as a function of incident light intensity (I) is plotted on a linear–log scale as shown in Figure 4B (bottom) for 60% and 80% Sn perovskite-based PVs. For bimolecular charge carrier recombination, this ideality factor n approaches unity. Whereas, when the ideality factor n approaches 2, Shockley–Read–Hall (SRH) type, trap-assisted recombination dominates.[56–59] In the case of 60% Sn-based perovskite PV device, the slope of the fall in V_{OC} results in a δV_{OC} 1.77$(kT/q)\ln(I)$ at low incident light intensities (up to 20 mW cm^{-2}). Thus, resulting in $n \approx$ 1.77 indicates SRH type of recombination in this irradiation regime. However, at higher irradiance regime (between 20 and 200 mW cm^{-2}) that includes standard AM 1.5 (100 mW cm^{-2}), we observe δV_{OC} 0.93$(kT/q)\ln(I)$. Thus, resulting in $n \approx$ 0.93 indicates a bimolecular type of carrier recombination as demonstrated previously for highly efficient CH$_3$NH$_3$PbI$_3$-based perovskite PVs.[32,57–59] This further confirms that at AM 1.5 intensities, traps can be filled at thermal equilibrium condition, where the overall recombination is mainly due to bimolecular processes and that trap states do not affect the charge transport enabling us to achieve high PCEs of ≈10% and V_{OC}'s close to the prediction of the S–Q model. However, for the 80% Sn content based perovskite PV, we observe only one regime from 1 to 200 mW cm^{-2} where δV_{OC} 1.95$(kT/q)\ln(I)$. Thus, resulting in an $n = 1.95$ indicates an SRH type trap-assisted charge carrier recombination process even at AM 1.5 intensities. This could be a result of a higher electronic disorder in 80% Sn perovskites compared to 60% Sn counterparts and moreover, the poor coverage (see the Supporting Information, Figure S9) would result in more grain boundaries and, hence, defects. Combined with the aforementioned light intensity dependence of J_{SC}, the poor performance of 80% Sn-based perovskite PV devices is expected compared to their 60% Sn counterparts.

In summary, we have presented a comprehensive study correlating the structural and photophysical properties of CH$_3$NH$_3$(Pb$_x$Sn$_{1-x}$)I$_3$ [0 ≤ x ≤ 1] perovskites. By substituting Sn with Pb, the bandgap shows an anomalous bowing effect and leads to lower bandgap (<1.2 eV) perovskites than the pure Sn-based perovskite—CH$_3$NH$_3$SnI$_3$. Using a novel elevated temperature processing method, we demonstrate uniform Sn–Pb-based low-bandgap perovskite thin films. We also highlight the importance of different ways to measure sensitive absorption and the differences in the results obtained, leading to quite contrary interpretations in the case of particular semiconductors. We

use the Sn–Pb-based perovskite thin films in fabricating highly efficient PVs using planar heterojunction architecture. The PV devices using 60% and 80% Sn content materials with bandgaps of ≈ 1.27 and 1.19 eV, respectively, demonstrated high PCEs. PCEs reaching about 10% and V_{OC}'s approaching the prediction of the S–Q model were realized after accounting for the losses incurred due to nonradiative recombination and entropy loss. These performances lead us to the conclusion that high charge carrier mobilities are essential to overcome the losses due to recombination as seen in these perovskites to help achieve high efficiencies. These high-performance low-bandgap perovskites could potentially open up new optoelectronic applications in NIR LEDs, lasers, and photodetectors.[27] Besides, they can also be potentially employed in all perovskite tandem or singlet fission PV architectures,[60,61] which promise to exceed the S–Q limit.

Experimental Section

CH$_3$NH$_3$(Pb$_x$Sn$_{1-x}$)I$_3$ [0 ≤ x ≤ 1] Perovskite Precursors Preparation: CH$_3$NH$_3$PbI$_3$ precursor solution was synthesized by dissolving lead iodide (PbI$_2$) and MACl in a 1:1 molar stoichiometric ratio in N,N-dimethylformamide to obtain a 0.15 M solution, and CH$_3$NH$_3$SnI$_3$ precursor solution was prepared from tin iodide (SnI$_2$) and MAI instead. The mixture, CH$_3$NH$_3$(Pb$_x$Sn$_{1-x}$)I$_3$ [0 ≤ x ≤ 1] perovskite precursors, was prepared by mixing the corresponding ratio of pure lead and tin perovskite precursor solutions.

Device Fabrication: Prepatterned ITO substrates were cleaned with acetone followed by isopropanol in an ultrasonic bath for 10 min each, after which the cleaned substrates were treated under oxygen plasma for 10 min. PEDOT:PSS solution was then spun at 3000 RPM for 60 s and annealed at 180 °C in nitrogen for 10 min. After 10 min of annealing PEDOT:PSS, the temperature of hotplate was increased to 240 °C, which was prepared for elevated temperature processing. CH$_3$NH$_3$(Pb$_x$Sn$_{1-x}$)I$_3$ [0 ≤ x ≤ 1] perovskite precursor solutions were also heated on another hotplate at 80 °C. Then the perovskite film was made in the nitrogen filled glovebox by loading CH$_3$NH$_3$(Pb$_x$Sn$_{1-x}$)I$_3$ [0 ≤ x ≤ 1] perovskite precursor solutions on substrates with PEDOT:PSS taken from hotplate up to 240 °C and subsequently spinning at 4000 RPM for 10 s and shifting immediately to hotplate at 100 °C for 10 min. On top of perovskite layer, PC$_{61}$BM was spun at 1500 RPM for 60 s from a 20 mg mL^{-1} solution in chlorobenzene. In the end, 100 nm aluminum was evaporated as the top electrode using thermal evaporation.

Photovoltaic Characterization: All the photovoltaic measurements were done using an air-free device holder where devices sit in a nitrogen atmosphere. Photocurrent density–voltage (J–V) measurements were carried out using a Keithley 2636A source-measure unit in the dark and under a Class A-Oriel 92250A solar simulator, after correcting for spectral mismatch using a calibrated reference solar cell from Fraunhofer Institute for Solar Energy Systems ISE (RS-OD4, SNo. 036–2011). The mismatch factor for such correction was obtained from the EQE measurements. All measurements apart from the intensity-dependent measurements were carried out under AM 1.5 illumination at 100 mW cm^{-2}. Light-intensity-dependent measurements were carried out under the same solar simulator using a combination of a series of attenuators (23%–100%) that changes the light level of the solar simulator (0.02–1 sun). The measurements from 1 to 10 sun were done using focusing lenses to increase the irradiation intensity. All the J–V measurements were done using a scan speed of 10 mV s^{-1} and physical mask that defines the pixel area of 4.5 mm^2. More than 35 devices were tested for the 60% and 80% Sn content PV devices.

EQE measurements were performed to measure the photoresponse as a function of photon energy using light from an Oriel Cornerstone 260 monochromator. EQEs were calculated from this, comparing the solar cell photoresponse to the response from a reference diode.

**ADVANCED
SCIENCE NEWS**
www.advancedsciencenews.com

**ADVANCED
MATERIALS**
www.advmat.de

COMMUNICATION

X-Ray Diffraction: $CH_3NH_3(Pb_xSn_{1-I})I_3$ $[0 \leq x \leq 1]$ perovskite films were prepared by the same recipe as in the device fabrication, spun the hot desired mixture solution precursor at 4000 for 10 s on substrates maintained on hotplate up to 240 °C. In order to protect perovskite films in air, another layer of PMMA was spun at 1000 for 60 s. Powder diffraction experiments were carried out on a PANalytical Empyrean Series 2 Diffractometer System with CuKα radiation (λ = 1.540598 Å, 1.544340 Å) over a 2θ range of 10°–60° with a step size of $2\theta = 0.0167°$. Quantitative analysis to determine the symmetry and lattice parameters was carried out using a Le Bail analysis,[40] in TOPAS version 5.[62]

Photothermal Deflection Spectroscopy (PDS): PDS is a highly sensitive surface averaged absorption measurement technique. For the measurements, a monochromatic pump light beam produced by a combination of a Light Support MKII 100 W xenon arc source and a CVI DK240 monochromator is shined on the sample (film on the quartz substrate), inclined perpendicular to the plane of the sample, which on absorption produces a thermal gradient near the sample surface via nonradiative relaxation induced heating. This results in a refractive index gradient in the area surrounding the sample surface. This refractive index gradient is further enhanced by immersing the sample in a deflection medium comprising of an inert liquid FC-72 Fluorinert (3M Company) which has a high refractive index change per unit change in temperature. A fixed wavelength continous wave (CW) transverse laser probe beam, produced using a Qioptiq 670 nm fiber-coupled diode laser with temperature stabilizer for reduced beam pointing noise, was passed through the thermal gradient in front of the sample producing a deflection proportional to the absorbed light at that particular wavelength, which was detected by a differentially amplified quadrant photodiode and a Stanford Research SR830 lock-in amplifier combination. Scanning through different wavelengths gave us the complete absorption spectra.

PL and PLQE Measurements: The PL and PLQE of thin-film samples were measured using an integrating sphere method, described elsewhere.[63] A continuous-wave 407 nm blue diode laser with an excitation power of 30 mW and a focused beam spot of ≈ 0.3 mm^2 was used to excite the samples optically. Emission was measured using an Andor iDus DU490A InGaAs detector. The samples were encapsulated between two glass cover slips before measurements.

Grazing-Incidence Wide-Angle X-ray Scattering (GIWAXS): Samples were measured in a grazing-incidence geometry at beamline I07 of the Diamond Light Source (Harwell, UK). A beam energy of 10 keV was used with samples housed in a custom-built chamber during measurement. Samples were tilted at 0.16° into the path of the incident X-rays. X-ray scatter was measured using a Pilatus 2M detector, calibrated using silver behenate powder. Collected data were analyzed using the DAWN software package (http://www.dawnsci.org/).

Terahertz: Terahertz time domain spectroscopy in the range 0.1–2 THz was carried out on encapsulated perovskites samples made on quartz substrates with different Sn content, under ambient conditions. The measurements were done using the Tera K15- T-Light MENLO system, with 60 mW pump pulse focused to a 40 μm spot onto the terahertz emitter, resulting in a broadband terahertz emission, with a spot size of ≈ 1 mm. The sample was placed between the terahertz source and the detector at normal incidence, and data were acquired at an integration time of 100 ms. Phase difference with respect to a reference quartz substrate was deduced from the Fourier transform of the primary transmitted peak (through perovskites) in the time domain. Normalization measurement was achieved on a blank reference quartz substrate separately. Multiple reflections within the substrate result in Fabry–Pérot fringes which were carefully removed by selecting only the first transmission peak in the time domain.

Supporting Information

Supporting Information is available from the Wiley Online Library or from the author.

[1] M. M. Lee, J. Teuscher, T. Miyasaka, T. N. Murakami, H. J. Snaith, *Science* **2012**, *338*, 643.

[2] M. Liu, M. B. Johnston, H. J. Snaith, *Nature* **2013**, *501*, 395.

[3] J. Burschka, N. Pellet, S.-J. Moon, R. Humphry-Baker, P. Gao, M. K. Nazeeruddin, M. Gratzel, *Nature* **2013**, *499*, 316.

[4] W. S. Yang, J. H. Noh, N. J. Jeon, Y. C. Kim, S. Ryu, J. Seo, S. I. Seok, *Science* **2015**, *348*, 1234.

[5] Efficiency chart, National Renewable Energy Laboratory, http://www.nrel.gov/ncpv/images/efficiency_chart.jpg, **2016**.

[6] A. Sadhanala, F. Deschler, T. H. Thomas, S. E. Dutton, K. C. Goedel, F. C. Hanusch, M. L. Lai, U. Steiner, T. Bein, P. Docampo, D. Cahen, R. H. Friend, *J. Phys. Chem. Lett.* **2014**, *5*, 2501.

[7] M. A. Green, K. Emery, Y. Hishikawa, W. Warta, E. D. Dunlop, *Prog. Photovoltaics Res. Appl.* **2016**, *24*, 3.

[8] M. A. Green, A. Ho-Baillie, H. J. Snaith, *Nat. Photonics* **2014**, *8*, 506.

[9] Z.-K. Tan, R. S. Moghaddam, M. L. Lai, P. Docampo, R. Higler, F. Deschler, M. Price, A. Sadhanala, L. M. Pazos, D. Credgington, F. Hanusch, T. Bein, H. J. Snaith, R. H. Friend, *Nat. Nanotechnol.* **2014**, *9*, 687.

[10] F. Deschler, M. Price, S. Pathak, L. E. Klintberg, D. D. Jarausch, R. Higler, S. Hüttner, T. Leijtens, S. D. Stranks, H. J. Snaith, M. Atatüre, R. T. Phillips, R. H. Friend, *J. Phys. Chem. Lett.* **2014**, *5*, 1421.

[11] X. Y. Chin, D. Cortecchia, J. Yin, A. Bruno, C. Soci, *Nat. Commun.* **2015**, *6*, 7383.

[12] A. Sadhanala, S. Ahmad, B. Zhao, N. Giesbrecht, P. M. Pearce, F. Deschler, R. L. Z. Hoye, K. C. Gödel, T. Bein, P. Docampo, S. E. Dutton, M. F. L. De Volder, R. H. Friend, *Nano Lett.* **2015**, *15*, 6095.

[13] F. Hao, C. C. Stoumpos, D. H. Cao, R. P. H. Chang, M. G. Kanatzidis, *Nat. Photonics* **2014**, *8*, 489.

[14] N. K. Noel, S. D. Stranks, A. Abate, C. Wehrenfennig, S. Guarnera, A.-A. Haghighirad, A. Sadhanala, G. E. Eperon, S. K. Pathak, M. B. Johnston, A. Petrozza, L. M. Herz, H. J. Snaith, *Energy Environ. Sci.* **2014**, *7*, 3061.

[15] N. K. Kumawat, A. Dey, K. L. Narasimhan, D. Kabra, *ACS Photonics* **2015**, *2*, 349.

[16] C. C. Stoumpos, L. Frazer, D. J. Clark, Y. S. Kim, S. H. Rhim, A. J. Freeman, J. B. Ketterson, J. I. Jang, M. G. Kanatzidis, *J. Am. Chem. Soc.* **2015**, *137*, 6804.

[17] S. Nagane, U. Bansode, O. Game, S. Chhatre, S. Ogale, *Chem. Commun.* **2014**, *50*, 9741.

COMMUNICATION

[18] W. Zhang, G. E. Eperon, H. J. Snaith, *Nat. Energy* **2016**, *1*, 16048.

[19] S. D. Stranks, H. J. Snaith, *Nat. Nanotechnol.* **2015**, *10*, 391.

[20] C. Wehrenfennig, G. E. Eperon, M. B. Johnston, H. J. Snaith, L. M. Herz, *Adv. Mater.* **2014**, *26*, 1584.

[21] Y. Mei, C. Zhang, Z. V. Vardeny, O. D. Jurchescu, *MRS Commun.* **2015**, *5*, 297.

[22] A. Miyata, A. Mitioglu, P. Plochocka, O. Portugall, J. T.-W. Wang, S. D. Stranks, H. J. Snaith, R. J. Nicholas, *Nat. Phys.* **2015**, *11*, 582.

[23] S. D. Stranks, V. M. Burlakov, T. Leijtens, J. M. Ball, A. Goriely, H. J. Snaith, *Phys. Rev. Appl.* **2014**, *2*, 034007.

[24] K. Galkowski, A. Mitioglu, A. Miyata, P. Plochocka, O. Portugall, G. E. Eperon, J. T.-W. Wang, T. Stergiopoulos, S. D. Stranks, H. Snaith, R. J. Nicholas, *Energy Environ. Sci.* **2016**, *9*, 962.

[25] G. Li, Z.-K. Tan, D. Di, M. L. Lai, L. Jiang, J. H. Lim, R. H. Friend, N. C. Greenham, *Nano Lett.* **2015**, *15*, 2640.

[26] G. Li, F. W. R. Rivarola, N. J. L. K. Davis, S. Bai, T. C. Jellicoe, F. de la Peña, S. Hou, C. Ducati, F. Gao, R. H. Friend, N. C. Greenham, Z.-K. Tan, *Adv. Mater.* **2016**, *28*, 3528.

[27] H. Cho, S.-H. Jeong, M.-H. Park, Y.-H. Kim, C. Wolf, C.-L. Lee, J. H. Heo, A. Sadhanala, N. Myoung, S. Yoo, S. H. Im, R. H. Friend, T.-W. Lee, *Science* **2015**, *350*, 1222.

[28] H. Zhu, Y. Fu, F. Meng, X. Wu, Z. Gong, Q. Ding, M. V. Gustafsson, M. T. Trinh, S. Jin, X.-Y. Zhu, *Nat. Mater.* **2015**, *14*, 636.

[29] D. H. Cao, C. C. Stoumpos, O. K. Farha, J. T. Hupp, M. G. Kanatzidis, *J. Am. Chem. Soc.* **2015**, *137*, 7843.

[30] F. Zuo, S. T. Williams, P.-W. Liang, C.-C. Chueh, C.-Y. Liao, A. K.-Y. Jen, *Adv. Mater.* **2014**, *26*, 6454.

[31] F. Hao, C. C. Stoumpos, R. P. H. Chang, M. G. Kanatzidis, *J. Am. Chem. Soc.* **2014**, *136*, 8094.

[32] W. Nie, H. Tsai, R. Asadpour, A. J. Neukirch, G. Gupta, J. J. Crochet, M. Chhowalla, S. Tretiak, M. A. Alam, H. Wang, **2015**, *347*, 522.

[33] J. Im, C. C. Stoumpos, H. Jin, A. J. Freeman, M. G. Kanatzidis, *J. Phys. Chem. Lett.* **2015**, *6*, 3503.

[34] S. De Wolf, J. Holovsky, S.-J. Moon, P. Löper, B. Niesen, M. Ledinsky, F.-J. Haug, J.-H. Yum, C. Ballif, *J. Phys. Chem. Lett.* **2014**, *5*, 1035.

[35] W. Zhang, S. Pathak, N. Sakai, T. Stergiopoulos, P. K. Nayak, N. K. Noel, A. A. Haghighirad, V. M. Burlakov, D. W. DeQuilettes, A. Sadhanala, W. Li, L. Wang, D. S. Ginger, R. H. Friend, H. J. Snaith, *Nat. Commun.* **2015**, *6*, 10030.

[36] A. Sadhanala, A. Kumar, S. Pathak, A. Rao, U. Steiner, N. C. Greenham, H. J. Snaith, R. H. Friend, *Adv. Electron. Mater.* **2015**, *1*, 1500008.

[37] W. Rieger, R. Dimitrov, D. Brunner, E. Rohrer, O. Ambacher, M. Stutzmann, *Phys. Rev. B* **1996**, *54*, 17596.

[38] F. Deschler, M. Price, S. Pathak, L. E. Klintberg, D.-D. Jarausch, R. Higler, S. Hüttner, T. Leijtens, S. D. Stranks, H. J. Snaith, M. Atatüre, R. T. Phillips, R. H. Friend, *J. Phys. Chem. Lett.* **2014**, *5*, 1421.

[39] C. C. Stoumpos, C. D. Malliakas, M. G. Kanatzidis, *Inorg. Chem.* **2013**, *52*, 9019.

[40] A. Le Bail, H. Duroy, J. L. Fourquet, *Mater. Res. Bull.* **1988**, *23*, 447.

[41] J. Rodriguez-Carvajal, M. T. Fernandez-Diaz, J. L. Martinez, *J. Phys. Condens. Matter* **1991**, *3*, 3215.

[42] A. M. Glazer, *IUCr, Acta Crystallogr., Sect. B: Struct. Crystallogr. Cryst. Chem.* **1972**, *28*, 3384.

[43] R. H. Mitchell, *Perovskites: Modern and Ancient*, Almaz Press, Thunder Bay, ON, Canada **2002**.

[44] H. T. Stokes, E. H. Kisi, D. M. Hatch, C. J. Howard, *Acta Crystallogr., Sect. B: Struct. Sci.* **2002**, *58*, 934.

[45] G. Lin, Y. Lin, H. Huang, R. Cui, X. Guo, B. Liu, J. Dong, X. Guo, B. Sun, *Nano Energy* **2016**, *27*, 638.

[46] Y. Li, W. Sun, W. Yan, S. Ye, H. Rao, H. Peng, Z. Zhao, Z. Bian, Z. Liu, H. Zhou, C. Huang, *Adv. Energy Mater.* **2016**, DOI: 10.1002/201601353.

[47] W. Liao, D. Zhao, Y. Yu, N. Shrestha, K. Ghimire, C. R. Grice, C. Wang, Y. Xiao, A. J. Cimaroli, R. J. Ellingson, N. J. Podraza, K. Zhu, R.-G. Xiong, Y. Yan, *J. Am. Chem. Soc.* **2016**, *138*, 12360.

[48] C.-G. Wu, C.-H. Chiang, Z.-L. Tseng, M. K. Nazeeruddin, A. Hagfeldt, M. Grätzel, *Energy Environ. Sci.* **2015**, *8*, 2725.

[49] D. Bi, W. Tress, M. I. Dar, P. Gao, J. Luo, C. Renevier, K. Schenk, A. Abate, F. Giordano, J.-P. Correa Baena, J.-D. Decoppet, S. M. Zakeeruddin, M. K. Nazeeruddin, M. Gra tzel, A. Hagfeldt, *Sci. Adv.* **2016**, *2*, e1501170.

[50] H. Tsai, W. Nie, P. Cheruku, N. H. Mack, P. Xu, G. Gupta, A. D. Mohite, H.-L. Wang, *Chem. Mater.* **2015**, *27*, 5570.

[51] O. D. Miller, E. Yablonovitch, S. R. Kurtz, *IEEE J. Photovoltaics* **2012**, *2*, 303.

[52] P. K. Nayak, D. Cahen, *Adv. Mater.* **2014**, *26*, 1622.

[53] R. T. Ross, *J. Chem. Phys.* **1967**, *46*, 4590.

[54] L. J. A. Koster, V. D. Mihailetchi, H. Xie, P. W. M. Blom, *Appl. Phys. Lett.* **2005**, *87*, 1.

[55] D. Bi, L. Yang, G. Boschloo, A. Hagfeldt, E. M. J. Johansson, *J. Phys. Chem. Lett.* **2013**, *4*, 1532.

[56] L. J. A. Koster, V. D. Mihailetchi, R. Ramaker, P. W. M. Blom, *Appl. Phys. Lett.* **2005**, *86*, 123509.

[57] D. Zhao, M. Sexton, H.-Y. Park, G. Baure, J. C. Nino, F. So, *Adv. Energy Mater.* **2015**, *5*, 1401855.

[58] J.-C. Blancon, W. Nie, A. J. Neukirch, G. Gupta, S. Tretiak, L. Cognet, A. D. Mohite, J. J. Crochet, *Adv. Funct. Mater.* **2016**, *26*, 4283.

[59] N. Marinova, W. Tress, R. Humphry-Baker, M. I. Dar, V. Bojinov, S. M. Zakeeruddin, M. K. Nazeeruddin, M. Grätzel, *ACS Nano* **2015**, *9*, 4200.

[60] B. Ehrler, M. W. B. Wilson, A. Rao, R. H. Friend, N. C. Greenham, *Nano Lett.* **2012**, *12*, 1053.

[61] D. N. Congreve, J. Lee, N. J. Thompson, E. Hontz, S. R. Yost, P. D. Reusswig, M. E. Bahlke, S. Reineke, T. Van Voorhis, M. A. Baldo, *Science* **2013**, *340*, 334.

[62] A. A. Coelho, J. Evans, I. Evans, A. Kern, S. Parsons, *Powder Diffr.* **2011**, *26*, S22.

[63] J. C. de Mello, H. F. Wittmann, R. H. Friend, *Adv. Mater.* **1997**, *9*, 230.

[64] A. T. Barrows, S. Lilliu, A. J. Pearson, D. Babonneau, A. D. F. Dunbar, D. G. Lidzey, *Adv. Funct. Mater.* **2016**, *26*, 4934.

[65] M. Nakajima, N. Takubo, Z. Hiroi, Y. Ueda, T. Suemoto, *Appl. Phys. Lett.* **2008**, *92*, 011907.

[66] R. Degl'Innocenti, D. S. Jessop, C. W. O. Sol, L. Xiao, S. J. Kindness, H. Lin, J. A. Zeitler, P. Braeuninger-Weimer, S. Hofmann, Y. Ren, V. S. Kamboj, J. P. Griffiths, H. E. Beere, D. A. Ritchie, *ACS Photonics* **2016**, *3*, 464.

[67] S. Funk, G. Acuna, M. Handloser, R. Kersting, *Opt. Express* **2009**, *17*, 17450.

[68] E. Mosconi, P. Umari, F. De Angelis, *J. Mater. Chem. A* **2015**, *3*, 9208.